Key Points:
- A log maximum likelihood method was used to determine end-member compositions of a fracture in Marathon Valley, Endeavour crater, Mars
- A Mg-sulfate-rich soil end-member and hematite-rich pebbles in the fracture imply alteration in an acid-sulfate environment
- Results add to growing evidence of alteration along the rim of Endeavour crater by enhanced fluid flow along fracture zones

Correspondence to:
N. T. Stein,
nstein@caltech.edu

Retrieval of Compositional End-Members From Mars Exploration Rover Opportunity Observations in a Soil-Filled Fracture in Marathon Valley, Endeavour Crater Rim

N. T. Stein[1] (iD), R. E. Arvidson[2] (iD), J. A. O'Sullivan[3], J. G. Catalano[2] (iD), E. A. Guinness[2] (iD), D. V. Politte[3] (iD), R. Gellert[4] (iD), and S. J. VanBommel[4] (iD)

[1]Division of Geological and Planetary Sciences, California Institute of Technology, Pasadena, CA, USA, [2]Department of Earth and Planetary Sciences, Washington University in Saint Louis, Saint Louis, MO, USA, [3]Department of Electrical Engineering, Washington University in Saint Louis, Saint Louis, MO, USA, [4]Department of Physics, University of Guelph, Guelph, ON, Canada

Abstract The Opportunity rover investigated a gentle swale on the rim of Endeavour crater called Marathon Valley where a series of bright planar outcrops are cut into polygons by fractures. A wheel scuff performed on one of the soil-filled fracture zones revealed the presence of three end-members identified on the basis of Pancam multispectral imaging observations covering ~0.4 to 1 μm: red and dark pebbles, and a bright soil clod. Multiple overlapping Alpha Particle X-ray Spectrometer (APXS) measurements were collected on three targets within the scuff zone. The field of view of each APXS measurement contained various proportions of the Pancam-based end-members. Application of a log maximum likelihood method for retrieving the composition of the end-members using the 10 APXS measurements shows that the dark pebble end-member is compositionally similar to average Mars soil, with slightly elevated S and Fe. In contrast, the red pebble end-member exhibits enrichments in Al and Si and is depleted in Fe and Mg relative to average Mars soil. The soil clod end-member is enriched in Mg, S, and Ni. Thermodynamic modeling of the soil clod end-member composition indicates a dominance of sulfate minerals. We hypothesize that acidic fluids in fractures leached and oxidized the basaltic host rock, forming the red pebbles, and then evaporated to leave behind sulfate-cemented soil.

Plain Language Summary The Opportunity rover investigated a region on the rim of Endeavour crater on Mars called Marathon Valley where a series of bright outcrops are cut by fractures. A scuff performed by one of the rover wheels on the fractures revealed the presence of three different compositional end-members. A novel technique was applied to retrieve the composition of the end-members using measurements by the rover's Alpha Particle X-ray Spectrometer and Pancam instruments. The presence of a magnesium-sulfate-rich soil end-member and hematite-rich pebbles in the scuffed fracture imply alteration in an acid-sulfate environment. Results add to growing evidence of alteration along the rim of Endeavour crater that was concentrated along fractures, which likely provided a conduit for subsurface fluid flow. The timing of formation of these altered deposits is unclear; they could have formed during transient postimpact hydrothermal activity or perhaps significantly later utilizing groundwater from the southern highlands.

1. Introduction

The Opportunity rover arrived at the western rim of Endeavour crater in August 2011. Opportunity's exploration of this highly degraded, 22 km diameter Noachian-age crater has focused on finding evidence for the interaction of water with rim materials, including implications for habitability (e.g., Arvidson et al., 2014, 2016; Squyres et al., 2012). The Cape York, Murray Ridge, and Cape Tribulation rim segments have been explored thus far (Figure 1). Traverses and measurements taken by Opportunity were in part directed based on findings from Mars Reconnaissance Orbiter Compact Reconnaissance Imaging Spectrometer for Mars (CRISM)-based hyperspectral observations, including detections of Fe^{3+} smectites on the eastern side of Cape York (Arvidson et al., 2014) and Fe^{3+}-Mg^{2+} smectites in a gentle swale called Marathon Valley (Figure 2) on Cape Tribulation (Fox et al., 2016). Ground-based measurements with the Opportunity rover during its kilometers of traversing on Endeavour's rim segments have included the acquisition of multispectral (13F, 0.43 to 0.98 μm) images using the Pancam camera system on the rover's mast (Bell III et al., 2006;
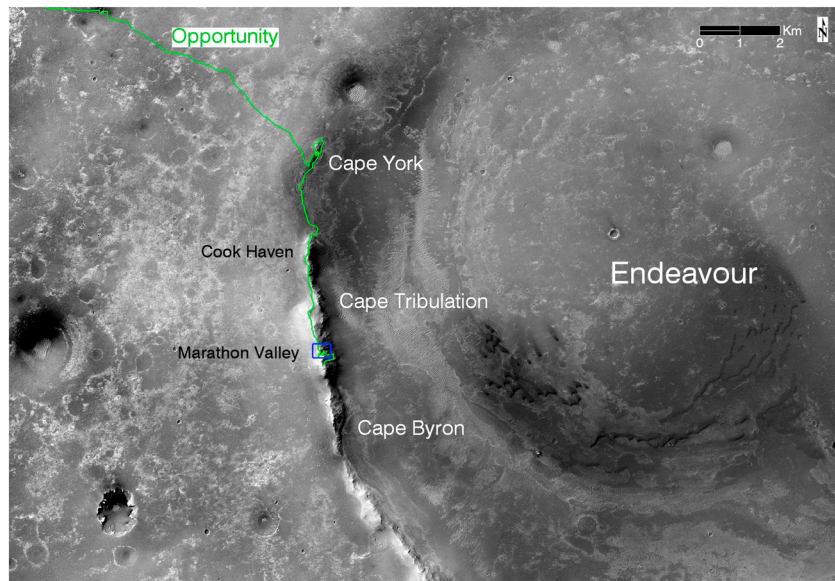
Figure 1. Portion of a Mars Reconnaissance Orbiter (MRO) context imager (CTX, Malin et al., 2007) frame covering the southwestern part of Endeavour crater, including rim segments traversed (green line) and examined by the Opportunity rover. The blue box delineates location of a portion of an MRO HiRISE image covering Marathon Valley shown in Figure 2, where Opportunity conducted extensive measurements, including in a soil-filled fracture scuffed by the rover's left front wheel. CTX frame f02_036753_1772_02s005w.tiff.

Farrand et al., 2016, 2017), together with Microscopic Imager (MI, 31 μm pixel widths) (Herkenhoff et al., 2003) and Alpha Particle X-Ray Spectrometer (APXS) measurements (Gellert et al., 2006; Mittlefehldt et al., 2016) using the Instrument Deployment Device (IDD) to place these two instruments onto soil and rock targets. The Rock Abrasion Tool, also located on the IDD, has been used to brush and/or abrade selected rock targets before acquisition of MI and APXS measurements (Gorevan et al., 2003).

Marathon Valley is 10–15 m deep, ~100 m wide, and strikes ~N60E across Cape Tribulation (Figure 2). It was the site of an extensive imaging and contact science measurement campaign (Crumpler et al., 2016;
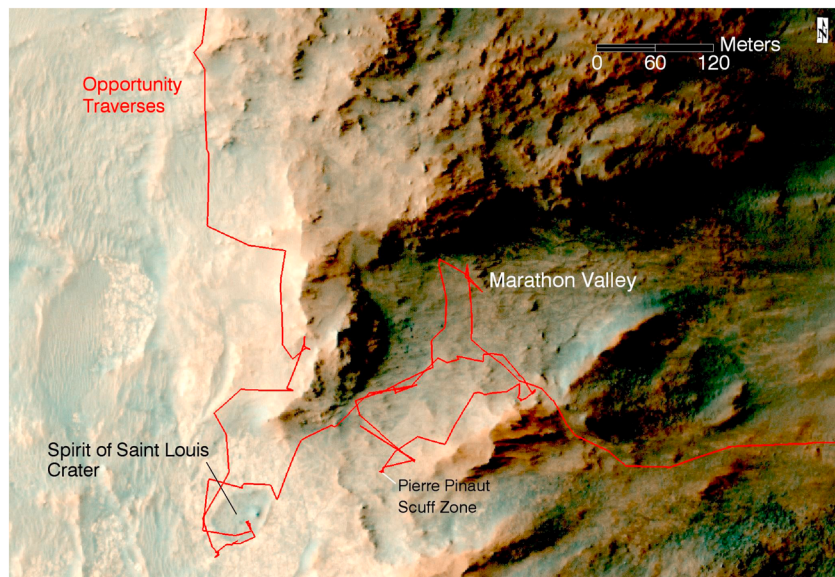
Figure 2. A portion of a HiRISE merged RGB image (McEwen et al., 2007) is shown covering Marathon Valley, located on Cape Tribulation. Opportunity entered Marathon Valley from the west near Spirit of Saint Louis Crater, acquired numerous remote sensing and contact science observations, and then entered Marathon Valley for another extensive set of measurements. One of the last measurement campaigns was on the bedrock target Pierre Pinaut and the nearby and scuffed soil-filled fracture. Image center location 2°18′53.76″S, 5°21′10.72″W. HiRISE frame ESP_036753_1775_MRGB_prj_v2.tiff.

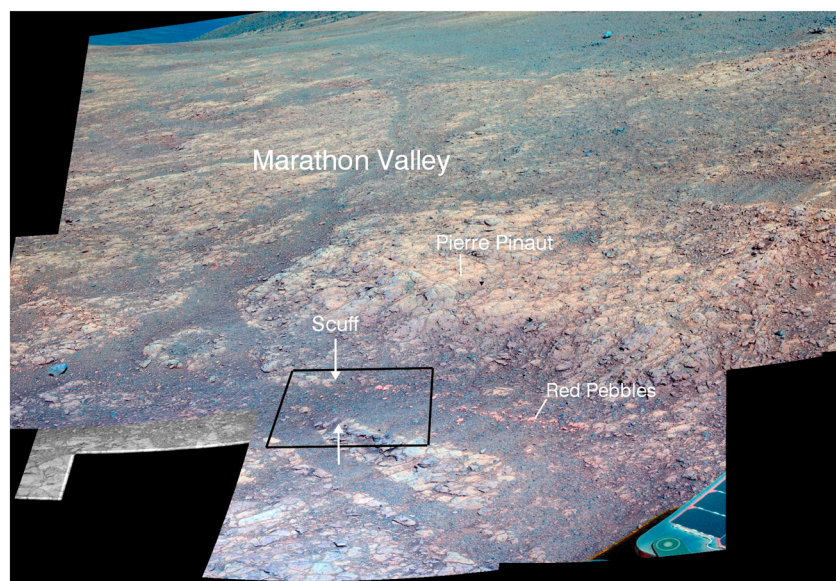**Figure 3.** Portion of a Pancam false color mosaic acquired within Marathon Valley looking toward the southeast at the breccia outcrops and fractures filled by dark soils. The location of the contact science target Pierre Pinaut and the scuffed soil-filled fracture are shown before work was done on these targets. The black box delineates postscuff Pancam image view shown in Figure 4. The white arrows denote the margins of the scuff. Note specifically the red pebbles within the scuffed fracture. RGB shown using bands L2 (0.753 μm), L5 (0.535 μm), and L7 (0.432 μm). Pancam mosaic was acquired using a number of individual frames on sol 4343.

Mittlefehldt et al., 2016). The entrance to Marathon Valley contains a shallow, flat-floored ~25 m diameter depression named Spirit of Saint Louis Crater (Figure 2). The depression is surrounded by an apron of bright planar outcrops cut into polygonal plates by fractures. These planar outcrops extend into Marathon Valley proper, and all of the planar outcrops are fine-grained impact breccias, likely a facies of the Shoemaker formation that dominates the outcrops on the western rim of Endeavour crater. The bulk compositions of the bedrock exposures found during Opportunity's extensive measurement campaign at Spirit of Saint Louis Crater and Marathon Valley are similar to that of Shoemaker formation outcrops encountered elsewhere on Cape York and Cape tribulation, with slight enrichments in Mg and S (Mittlefehldt et al., 2016). Clusters of red pebbles with enhanced Al and Si contents, some exhibiting Pancam-based hematite spectral signatures (~0.86 μm absorption, Farrand et al., 2017), were found within some of the fracture zones located between the planar outcrops (Mittlefehldt et al., 2016). The planar outcrops are also interpreted to be the carriers of a CRISM-based Fe^{3+}-Mg^{2+} smectite signature (Fox et al., 2016).

1.1. Scuff Zone Measurements

After completing in situ measurements on a number of outcrop targets within Marathon Valley, Opportunity conducted extensive work on the Pierre Pinaut outcrop target, including abrading the target using the rock abrasion tool (RAT), followed by MI and APXS measurements. Opportunity was then commanded to drag its left front wheel across a nearby soil-filled fracture zone with a cluster of red pebbles at its edge (Figures 3 and 4). The scuff exposed a mixture of relatively bright, colorful soil with portions cemented into clods (Figure 4). Ten APXS observations were collected on or near the scuff: three overlapping measurements of a cluster of red pebbles (target George Drouillard) within the fracture and adjacent to the scuff zone, three overlapping measurements of colorful soil within the wheel scuff (target E Cann), and four overlapping measurements centered on a soil clod (target Private Joseph Field) (Figures 4 and 5 and Table 1). In addition, Pancam 13 filter (13F) data were acquired for these targets after completion of the contact science measurements. In this paper, we solve for the compositions in locations with high areal abundances of Pancam-based spectral end-members by convolving the APXS fields of view (FOV) for the 10 measurements with areal abundance maps for spectral end-members generated from Pancam 13F image data. The intent is to retrieve compositions at a much finer scale than the ~4.25 cm diameter APXS FOV of the 10 measurements, with the underlying assumption that the Pancam spectral patterns correlate directly with compositional trends. We revisit this assumption and its validity in section 4 of the paper.
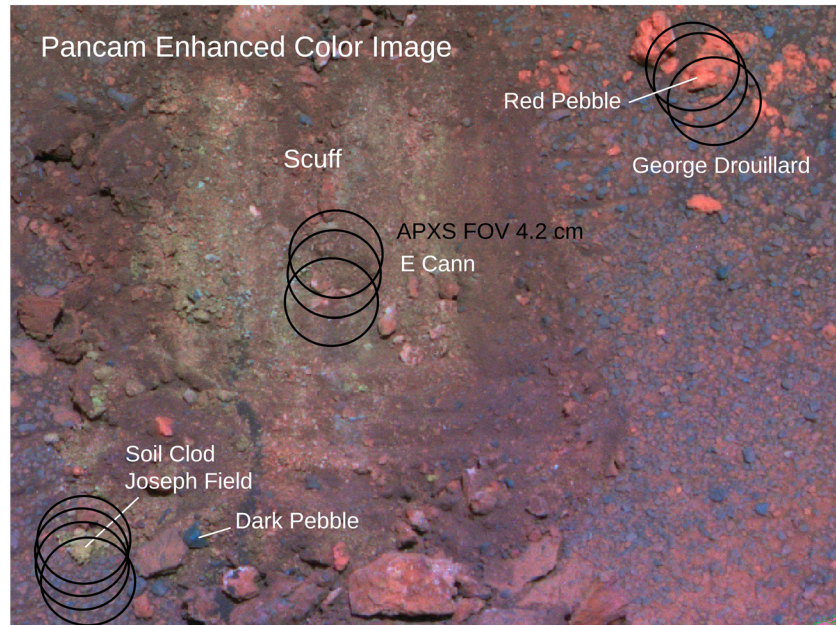
Figure 4. Pancam image acquired on sol 4404 of the scuff zone and red pebble targets showing each of the 10 APXS targets that were used to calculate end-member compositions. Red, green, and blue colors show the relative abundance of each end-member. R, Red pebbles; G, Bright soil; B, Dark pebbles. The APXS fields of view for E Cann, Private Joseph Field, and George Drouillard are shown as black circles. The E Cann measurements were collected near the center of the scuff axis and predominantly capture bright soil. The Private Joseph Field measurements primarily capture a bright soil clod. The George Drouillard measurements predominantly overlie a group of red pebbles.

2. Methodology

Previous efforts to resolve the compositions of fine-scale end-members in APXS observations (Arvidson et al., 2016) used Pancam 13F observations to retrieve spectral reflectance end-members for the Pinnacle and Stuart Island sulfate-bearing rocks excavated by Opportunity's wheels in a fracture in the Cook Haven area of Endeavour's rim. Pancam-based spectral end-member areal abundance maps were convolved with a matrix of oxide compositions from APXS observations to reproduce a transfer matrix whereby a given APXS observation was weighted by the relative areal abundances of the spectral end-members. In the absence of noise, postmultiplying the transfer function matrix by the matrix of end-member compositions would produce the matrix of observed compositions for each APXS measurement. Nonlinear least squares techniques were used in Arvidson et al. (2016) to solve for the end-member compositions. A similar
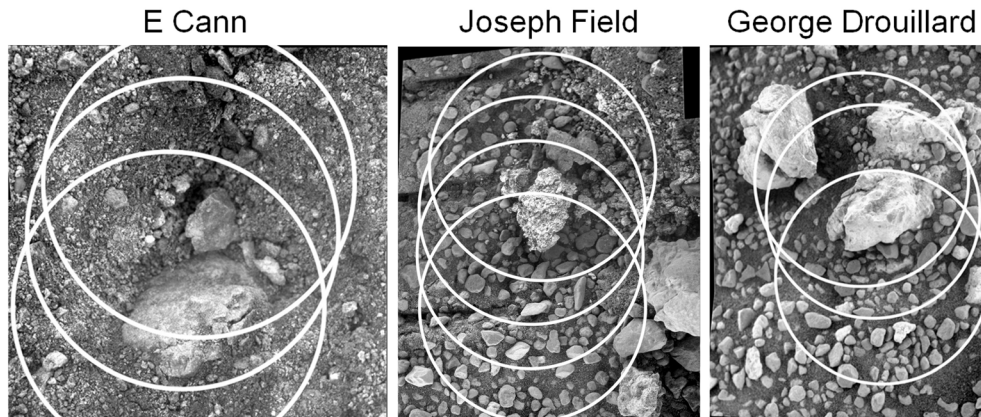
Figure 5. Microscopic Imager (MI) mosaics of the E Cann (bright excavated soil), Joseph Field (centered on bright soil clod located just above middle of the mosaic), and George Drouillard (cluster of three red pebbles) targets. APXS observations start with 1 and increase downward, for example, E Cann-1 is at the top and E Cann-3 at the bottom of the E Cann mosaic. White circles denote the areal extent of each APXS measurement, given the stand-off distances. In each, an APXS 100% field of view of 4.25 cm is shown, assuming an APXS stand-off distance of 1 cm above the surface.

Table 1
Compositions From Scuff Zone Measurements, Along With Associated Statistical Uncertainties

	Na₂O (wt %)	MgO (wt %)	Al₂O₃ (wt %)	SiO₂ (wt %)	P₂O₅ (wt %)	SO₃ (wt %)	Cl (wt %)	K₂O (wt %)	CaO (wt %)	TiO₂ (wt %)	Cr₂O₃ (wt %)	MnO (wt %)	FeO (wt %)	Ni (ppm)	Zn (ppm)	Br (ppm)
						Input APXS Measurements (D)										
E_Cann1	0.79	9.05	6.50	31.6	1.10	25.15	0.30	0.27	5.04	0.88	0.23	0.26	18.7	1203	169	58
E_Cann2	0.93	7.75	6.99	35.9	1.09	21.34	0.34	0.33	5.09	1.00	0.32	0.30	18.5	758	176	70
E_Cann3	0.82	10.14	6.16	32.9	0.98	24.51	0.31	0.28	4.61	0.93	0.30	0.35	17.4	1763	158	54
JosephField1	0.66	6.78	8.00	39.1	0.99	17.97	0.53	0.42	5.92	1.08	0.25	0.23	18.0	59	258	88
JosephField2	0.96	7.03	8.32	39.5	1.02	17.60	0.60	0.45	5.71	1.03	0.29	0.26	17.2	57	220	64
JosephField3	1.10	6.91	8.97	42.4	0.94	13.30	0.70	0.54	6.14	1.16	0.29	0.33	17.1	138	266	60
JosephField4	1.37	7.19	9.77	45.1	1.00	8.43	0.81	0.57	6.85	1.21	0.37	0.34	17.0	67	313	56
George_Drouillard1	1.16	5.97	9.92	52.5	1.27	8.69	1.21	0.42	5.99	1.17	0.37	0.26	11.0	145	102	262
George_Drouillard2	1.27	6.01	10.31	53.1	1.18	7.73	1.16	0.47	5.77	1.21	0.39	0.22	11.1	169	123	206
George_Drouillard3	1.43	6.57	10.04	49.9	1.04	6.52	0.89	0.51	6.43	1.15	0.38	0.25	14.8	204	187	94
Mars Average Soil	2.73	8.35	9.71	45.41	0.83	6.16	0.68	0.44	6.37	0.90	0.36	0.33	16.73	490	286	61
						Input APXS Errors (δD)										
E_Cann1	0.28	0.20	0.15	0.42	0.12	0.37	0.03	0.07	0.08	0.09	0.05	0.03	0.20	112	33	25
E_Cann2	0.31	0.18	0.14	0.38	0.10	0.24	0.02	0.06	0.06	0.09	0.04	0.02	0.14	66	19	18
E_Cann3	0.32	0.19	0.13	0.34	0.10	0.25	0.01	0.06	0.05	0.07	0.04	0.01	0.13	72	16	17
JosephField1	0.25	0.16	0.15	0.44	0.10	0.25	0.03	0.07	0.08	0.09	0.05	0.02	0.17	81	32	23
JosephField2	0.25	0.15	0.14	0.42	0.10	0.22	0.02	0.06	0.07	0.10	0.04	0.02	0.14	67	25	23
JosephField3	0.32	0.20	0.23	0.60	0.12	0.20	0.04	0.08	0.11	0.10	0.06	0.03	0.19	97	43	27
JosephField4	0.22	0.12	0.13	0.35	0.10	0.18	0.03	0.07	0.07	0.09	0.05	0.02	0.11	78	30	21
George_Drouillard1	0.26	0.15	0.16	0.53	0.10	0.14	0.03	0.06	0.07	0.08	0.04	0.02	0.10	56	18	22
George_Drouillard2	0.28	0.17	0.19	0.59	0.10	0.15	0.03	0.07	0.08	0.09	0.05	0.02	0.12	64	22	24
George_Drouillard3	0.28	0.20	0.15	0.42	0.12	0.37	0.03	0.07	0.08	0.09	0.05	0.03	0.20	112	33	25

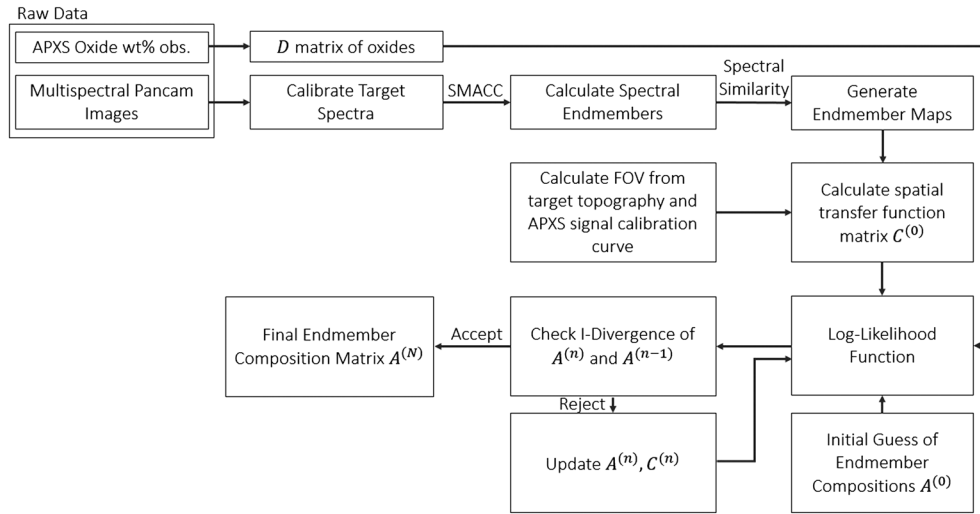*Note.* Mars average soil from *Taylor and McLennan* (2009).

Figure 6. Flowchart illustrating the end-member retrieval process. Inputs include the measured APXS oxide compositions for each target, multispectral Pancam images that are used to calculate the spatial distribution of end-member abundances, and an initial guess of end-member compositions. The outputs are the final transfer matrix $C^{(N)}$ and end-member composition matrix $A^{(N)}$.

technique has been applied to Curiosity rover APXS data in VanBommel et al. (2016, 2017), where compositional end-members were derived from visually distinct end-members in Mars Hand Lens Imager (MAHLI) images.

For the Marathon Valley observations in this paper, a log maximum likelihood approach is employed that allows iterative adjustment of both the transfer and end-member composition matrices to best match the observed compositional data. The log maximum likelihood approach offers some advantages over nonlinear least squares techniques. Most importantly, the log maximum likelihood method intrinsically allows iterative adjustment of both the transfer function matrix and the end-member composition matrix. The nonlinear least squares method fixes the former to solve for the latter and thus any errors in the transfer matrix propagate into end-member composition errors. The utility of adjusting both the transfer and end-member composition matrices compensates for uncertainties in Pancam-based end-member concentrations where a Pancam pixel might cover a fine-grained mixture of these end-members. In addition, running nonlinear least squares and the log maximum likelihood method approaches on the same data set shows that the latter performs better in estimating realistic values for elemental abundances for low concentration species, whereas nonlinear least squares techniques sometimes yield physically unrealistic null oxide abundances (e.g., the nonlinear least squares application in Arvidson et al., 2016). As a result, the uncertainties reported for the log maximum likelihood method are smaller than those yielded by nonlinear least squares techniques for low-abundance oxides (Arvidson et al., 2016).

The overall flow diagram for the log maximum likelihood approach is shown in Figure 6. Matrix $[D_{ij}]$ is defined as the oxide weight abundances, indexed by j, of each Poisson-distributed APXS measurement indexed by i. The raw counts yielded by APXS measurements are assumed to be Poisson distributed, that is, the emission of X-rays can be described with counting statistics, because particle emission events are independent and occur with a known constant frequency (Gellert et al., 2006). The final solution is a result of a nonlinear iterative algorithm and thus is a nonlinear function of the measurements. Matrix $[C_{ik}]$ describes the relative contribution of the kth end-member to the ith APXS measurement. The composition A_{kj} of each spectral end-member is calculated by solving the noninvertible linear matrix equation

$$\sum_k C_{ik}A_{kj} = D_{ij}. \tag{1}$$

2.1. Solution Method

Because the entries of $[C_{ik}]$ are relative abundances, the rows must sum to unity as

$$\sum_k C_{ik} = 1. \tag{2}$$

The algorithm alternately minimizes a cost function over the pair (A, C) subject to the sum constraints. An important algorithmic basis for our approach is nonnegative matrix factorization, introduced by Lee and Seung (1999, 2001). Independently, O'Sullivan (2000) introduced this algorithm as an information-geometry version of the singular value decomposition. The algorithm presented here is an extension, accounting for the constraint that the relative end-member abundances sum to 1. Csiszár's I-divergence (Csiszár, 1991) is used as the cost function. Minimizing the I-divergence is equivalent to maximizing the Poisson log-likelihood function. The probabilities $\pi_{k \mid ij}$ are used to represent the cost function in a variational manner as

$$
\begin{aligned}
\text{Cos}t &= \sum_i \sum_j \left(D_{ij} \ln \frac{D_{ij}}{\Sigma_k C_{ik} A_{kj}} - D_{ij} + \sum_k c_{ik} A_{kj} \right) \\
&= \min_{\pi \in P} \sum_i \sum_j \sum_k \left(\pi_{k|ij} D_{ij} \ln \frac{\pi_{k|ij} D_{ij}}{C_{ik} A_{kj}} - \pi_{k|ij} D_{ij} + C_{ik} A_{kj} \right).
\end{aligned}
\tag{3}
$$

where $P = \{\pi_{k \mid ij} \geq 0 : \sum_k \pi_{k \mid ij} = 1\}$. The value of the cost equals the minimum of the function in line 2 of equation (3) over the set P of probabilities of end-members for each oxide weight abundance and APXS measurement. Equation (3) seeks to minimize the cost iteratively. The minimization over the probabilities for given estimates $(A^{(n)}, C^{(n)})$ is straightforward. The minimization over (A, C) given estimates $\pi_{k \mid ij}^{(n)}$ is more complicated and involves Lagrange multipliers μ_i to enforce the sum constraint (2). Substituting the estimates $\pi_{k \mid ij}^{(n)}$ and simplifying, the relative abundances and end-members $C_{ik}^{(n)}$ and $A_{kj}^{(n)}$ are updated during each of N iterations as

$$A_{kj}^{(n+1)} = \frac{A_{kj}^{(n)}}{\Sigma_{i'} C_{i'k}^{(n)}} \Sigma_i \frac{C_{ik}^{(n)} D_{ij}}{\Sigma_{k'} C_{ik'}^{(n)} A_{k'j}^{(n)}}. \tag{4}$$

$$C_{ik}^{(n+1)} = \frac{C_{ik}^{(n)}}{\Sigma_{j'} A_{kj'}^{(n+1)} - \mu_i^{(n+1)}} \Sigma_j \frac{A_{kj}^{(n)} D_{ij}}{\Sigma_{k'} C_{ik'}^{(n)} A_{k'j}^{(n)}}. \tag{5}$$

The estimates converge to the final end-member oxide weight percentage matrix $A_{kj}^{(N)}$ and relative abundances $C_{ik}^{(N)}$. The Lagrange multiplier $\mu_i^{(n+1)}$ is chosen to enforce the constraint (2) at each iteration. Computation of the Lagrange multiplier is straightforward because, when viewed as a function of $\mu_i^{(n+1)}$, the values of $C_{ik}^{(n+1)}$ are convex and monotonically increase as $\mu_i^{(n+1)}$ increases from $-\infty$. The convergence of the solution is tracked using the value of the cost function (Csiszár's I-divergence). The number of iterations must be sufficient for the cost function to converge to a near-constant value.

2.2. Initialization

The transfer matrix is computed as the convolution of the Pancam-based abundance maps and the APXS field-of-view function for each APXS measurement

$$C_{ik}^{(0)} = \sum_l I_{il} M_{lk}, \tag{6}$$

where M is a matrix of spectral end-member abundance maps for pixels indexed by ? and I is the matrix whose ?? entry is the relative intensity of the APXS FOV for observation ? at Pancam end-member map location ?. The relative intensity of the MER APXS FOV was calibrated through laboratory and Mars-based testing (Gellert et al., 2006). Per equation (2), $C_{ik}^{(0)}$ is normalized to sum to unity. The end-member composition matrix $A_{kj}^{(0)}$ is first initialized with estimates of the relative proportions of oxide weight abundances. Initial estimates are based on APXS observations centered over the Joseph Feld bright pebble with its high S content, the George Drouillard red pebble target with the highest Al and Si values, and Mars average soil (Taylor & McLennan, 2009). After initialization, $C_{ik}^{(n)}$ and $A_{kj}^{(n)}$ are adjusted during each iteration to converge to the best match for the APXS measurements. As noted, these iterations allow changes in both $C_{ik}^{(n)}$ and $A_{kj}^{(n)}$.

2.3. Sensitivity of Solution

A key question in the methodology is the sensitivity of the final end-member compositions to initial conditions and measurement errors, both random and systematic. To explore errors in estimated end-member
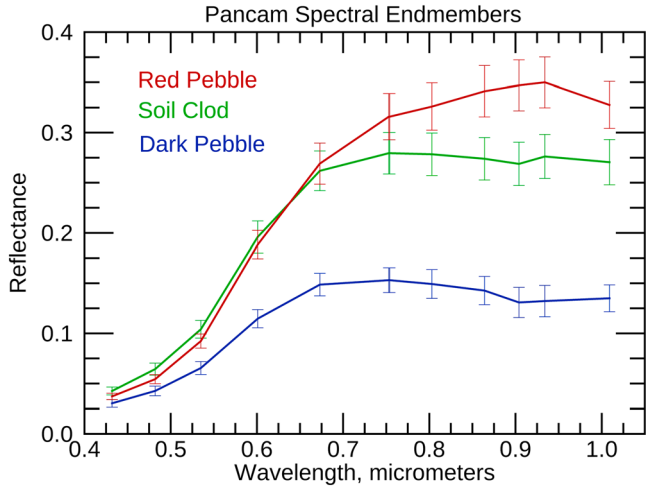
Pancam Spectral Endmembers

Figure 7. Pancam reflectance spectra of the red pebble, soil clod, and dark pebble end-members derived from linear unmixing as described in the text. Each spectrum is an average of several dozen pixels for relative areal abundances of >90%. Error bars represent 1 standard deviation in the spread of spectral values.

compositions, the nominal solution for $A^{(N)}$ is computed as above using the measured oxide weight abundance matrix D_{ij} that does not include statistical errors and is initialized with $C_{ik}^{(0)}$ from (6) and $A_{kj}^{(0)}$. Subsequently, the effect of variations of the input parameters on the computed compositional end-members is tracked by changing D_{ij}, $C_{ik}^{'(0)}$, and $A_{kj}^{'(0)}$ over a range of physically realistic quantities and computing new end-member compositions. To this end, a new transfer function matrix $C_{ik}^{'(0)}$ is initialized as a matrix of uniformly distributed random values as

$$C_{ik}^{'(0)} \sim U\left(\left[C_{ik}^{(N)} - \max_{ik}\left| C_{ik}^{(N)} - C_{ik}^{(0)} \right|, C_{ik}^{(N)} + \max_{ik}\left| C_{ik}^{(N)} - C_{ik}^{(0)} \right| \right] \right), \quad (7)$$

where $\max_{ik}\left| C_{ik}^{(N)} - C_{ik}^{(0)} \right|$ is the largest absolute difference between an element of the final and initial relative abundances (transfer functions). As a result, $C_{ik}^{'(0)}$ does not encompass every possible combination of relative abundances but instead samples from a subset of the total solution space encompassed by the difference between the final and initial transfer functions. Hence, it is possible that the reported uncertainties overestimate the accuracy of the solution if the true end-member abundances differ more significantly from $C^{(N)}$. Such a scenario is unlikely as the algorithm iteratively optimizes $C^{(N)}$ and $A^{(N)}$ to reach physically reasonable quantities. A new matrix of estimated end-member compositions is initialized as

$$A_{kj}^{'(0)} \sim U\left(\left[A_{kj}^{(0)} - \delta A_{kj}, A_{kj}^{(0)} + \delta A_{kj} \right] \right), \quad (8)$$

where δA_{kj} denotes a physically realistic range of values for A, taken here to be $0.5 A_{kj}^{(0)}$ (see section 3.1). New oxide abundances $D_{ij}^{'}$ are calculated as a matrix of uniformly distributed random values as

$$D_{ij}^{'} \sim U\left(\left[D_{ij} - \delta D_{ij}, D_{ij} + \delta D_{ij} \right] \right), \quad (9)$$

where δD_{ij} is a matrix of statistical errors for each oxide measurement. A new matrix of end-member compositions $A_{kj}^{'(N)}$ is computed using $D_{ij}^{'}$ and $C_{ik}^{'(0)}$. This computation is repeated over many (m, here approximately 10^4) trials to cover m permutations of $D_{ij}^{'}$ and $C_{ik}^{'(0)}$, yielding a matrix $A_{kjn}^{'(N)}$ containing m end-member compositions. The uncertainty δA_{kj} of the end-member solution is calculated as the maximum absolute difference between the nominal end-member solution $A_{kj}^{(N)}$ and $A_{kjn}^{'(N)}$ for each element as

$$\delta A_{kj} = \max_{n}\left| A_{kj}^{(N)} - A_{kjn}^{'(N)} \right|. \quad (10)$$

Figure 8. Average absolute change (wt %) in $A^{(N)}$ relative to the values of $A^{(n)}$ reported in Table 2 using different initial end-member compositions $A_{random}^{(0)}$. $A_{scuff}^{(0)}$ represents the initial end-member compositions used to derive the values in Table 2. The horizontal axis is the average % difference between values of randomly generated initial end-member compositions and $A_{scuff}^{(0)}$. No uncertainty is reported because this plot quantifies an average absolute change in the calculated values of $A^{(N)}$. This quantity is used in part to estimate the uncertainty of the final end-member solution (Table 2, see section 2.3).

3. Scuff Zone End-Member Retrieval

The first step in end-member retrieval is to determine spectral end-members from the Pancam observation covering the scuff area. Examination of Pancam color composites in approximate true color (RGB bands L2 (0.753 μm), L5 (0.535 μm), and L7 (0.432 μm), respectively) and MI images for the scuff zone and surroundings suggests the presence of three spectral end-members: red and dark pebbles and a bright soil clod excavated during the scuff and representative of bright, colorful soil exposed during the scuffing (Figures 4 and 5). This selection follows the standard approach used for selection of APXS targets for the Spirit, Opportunity, and Curiosity missions, that is, using color and textures to identify distinctive rocks and soils.

To quantitatively retrieve spectral end-members the following approach was used. First, extreme spectra defining the edges of the 13-dimension spectral space were identified and locations
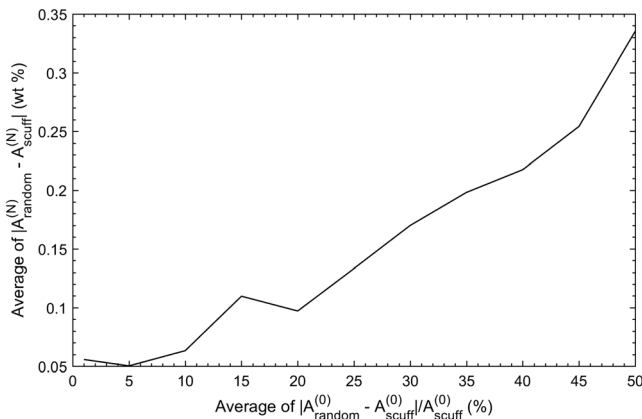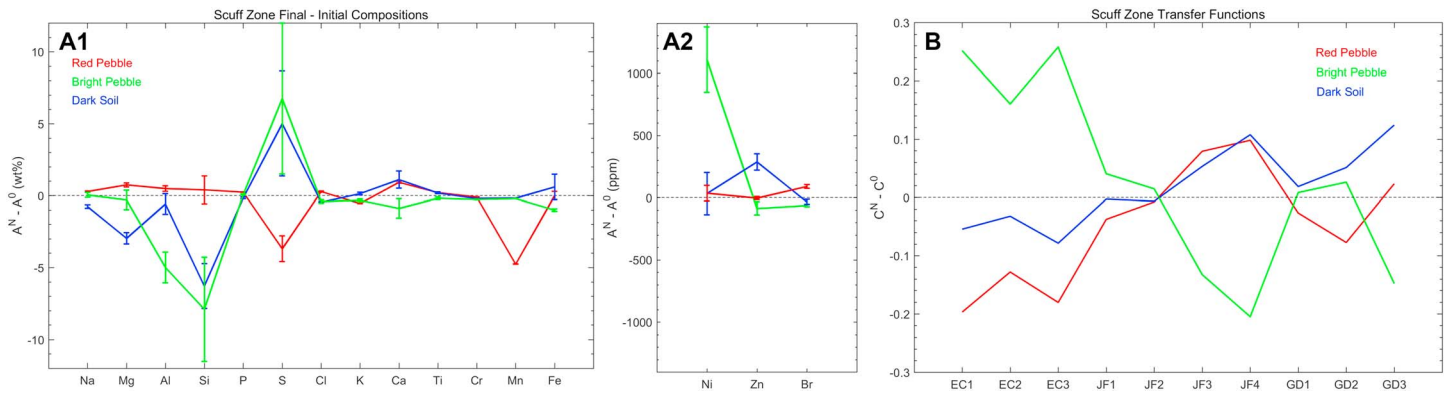
Figure 9. (a) Difference between final ($A^{(N)}$) and initial ($A^{(0)}$) compositions for each compositional end-member in (9a1) wt % or (9a2) ppm. The uncertainties are reported in Table 2. (b) Difference between final ($C^{(N)}$) and initial ($C^{(0)}$) transfer functions for each end-member. Changes relative to the initial transfer function are primarily attributed to inaccuracies in the end-member maps stemming from the spectral similarity of compositional end-members. Additional inaccuracies in the transfer function may arise from inaccuracies in estimates of APXS FOV size and location. The horizontal axis labels refer to different APXS targets (EC, E Cann; JF, Joseph Field; GD, George Drouillard). The uncertainties for the transfer function are not reported because this figure reports the average absolute change in the estimated quantities of $C^{(N)}$, which are used in part to estimate the uncertainty of the final end-member solution (section 2.3).

were mapped onto the Pancam image. Three end-members and a shadow spectrum were found and mapped directly to the visually identified targets: red and dark pebbles and the bright soil clod that corresponds to the Joseph Field target (Figure 4). A linear least squares unmixing procedure was then applied to the Pancam 13F image cube to retrieve concentration maps of the three end-members (Figure 4). The red pebble end-member maps spatially onto the George Drouillard red pebbles and the bright soil end-member onto the bright soil clod. The dark pebble end-member maps onto a dark pebble. Examination of residual error maps from the unmixing showed an RMS spatial mean of 0.004 and standard deviation about that mean of 0.002. Further, the RMS map was spatially bland. Both the magnitude and spatial distribution of the RMS errors indicate that three end-members and shadow account for the vast majority of variance in the Pancam 13F data. The shadow component was then removed, and the abundance of the three end-members in each pixel in the Pancam data was normalized to unity. We note that these end-members also correspond to color and textural end-members in the scene.

The dark pebble end-member shows a downturn at wavelengths longer than ~0.7 μm and an overall low reflectance, implying a spectral dominance of ferrous silicates such as pyroxene at the longer wavelengths and Fe^{3+} oxides at the shorter wavelengths (Figure 7). As noted, the red pebble end-member is located on one of the George Drouillard pebbles and the spectrum shows slightly enhanced 0.53 and 0.86 μm absorptions relative to the other two end-members, consistent with the presence of nano-phase iron oxides (see also Farrand et al., 2017). The bright soil clod shows a downturn at wavelengths longer than ~0.7 μm that has been interpreted by Farrand et al. (2017) to be indicative of the presence of a Fe-sulfate phase, although the limited number of bands and wavelength coverage precludes unique identification of specific mineral phases.

3.1. Retrieval of Compositional End-Members

Figure 10. Ratio of the red pebble, soil clod, and dark pebble end-member compositions to the estimated average Martian average soil composition of Taylor and McLennan (2009). The ratio values and error bars are calculated from the quantities in Table 2.

To retrieve end-member compositions, the APXS FOVs were convolved with the Pancam-based end-member maps as a function of nadir sensor standoff distance (~1 cm) and associated FOV extent, assuming negligible variations in topography. The FOV diameter for the varying APXS measurements is approximately 4–5 cm. Hence, we use 4.25 cm as an average FOV diameter for each measurement. Each APXS observation convolved with the spectral end-member maps was then used to populate the initial transfer function matrix
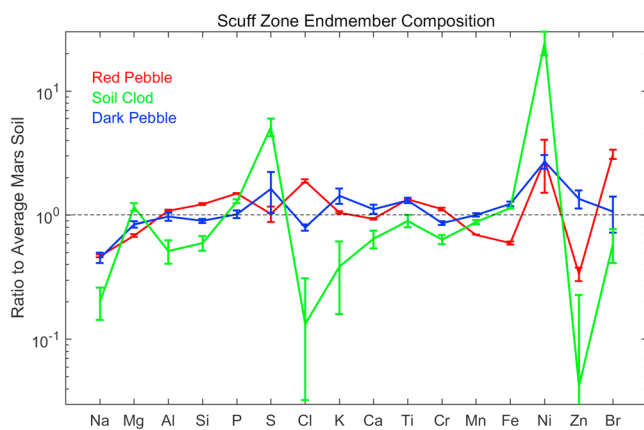
Table 2
Final End-Member Compositions and Associated Uncertainties From the Log Likelihood Method Assumed to Span the Solution Space of Physically Realistic Input Parameters $C^{(0)}$ and D

	Na$_2$O (wt %)	MgO (wt %)	Al$_2$O$_3$ (wt %)	SiO$_2$ (wt %)	P$_2$O$_5$ (wt %)	SO$_3$ (wt %)	Cl (wt %)	K$_2$O (wt %)	CaO (wt %)	TiO$_2$ (wt %)	Cr$_2$O$_3$ (wt %)	MnO (wt %)	FeO (wt %)	Ni (ppm)	Zn (ppm)	Br (ppm)
End-Member Composition (A)																
Red pebbles	1.28	5.74	10.49	55.39	1.24	6.31	1.28	0.46	5.92	1.21	0.40	0.23	10.01	136	96	189
Dark pebbles	1.24	7.03	9.42	40.71	0.84	10.00	0.54	0.63	7.11	1.18	0.31	0.33	20.60	132	386	65
Bright soil	0.55	9.70	5.00	27.10	1.07	31.75	0.09	0.17	4.11	0.81	0.23	0.29	18.99	1208	130	36
End-Member Composition Uncertainty (δA)																
Red pebbles	0.03	0.14	0.19	0.97	0.01	0.90	0.04	0.01	0.07	0.01	0.01	0.01	0.29	62	12	16
Dark pebbles	0.12	0.40	0.72	1.57	0.06	3.65	0.03	0.09	0.60	0.06	0.01	0.01	0.89	170	65	21
Bright soil	0.16	0.67	1.07	3.62	0.04	5.24	0.12	0.10	0.68	0.09	0.02	0.01	0.09	262	53	11

$C^{(0)}$. The end-member composition matrix $A^{(0)}$ was initialized with a best guess of the end-member compositions based on Pancam and APXS observations, with the process discussed used to estimate the initial end-member composition matrix for use in the iterative approach in which both the transfer and composition matrices can vary. Multiple trials confirm that altering the elements of $A^{(0)}$ by as much as 50% has a minimal effect on the reported values of $A^{(N)}$ (Figure 8), indicating that the choice of similar initial parameters would yield similar results. The final transfer function and end-member compositions were calculated using 10^4 iterations of the log-likelihood algorithm (Figures 9 and 10). The large difference between initial and final transfer matrix values for the E Cann targets (as much as ~30%) is interpreted to be due to challenging conditions for resolving the finely intermixed materials in the center of the scuff using Pancam spectra (Figures 4 and 7) and to a lesser extent from errors in the initial transfer function matrix due to uncertainties in the FOV placement and extent. The algorithm adjusts both the composition and transfer function matrices for these targets to converge to the optimum solution. Uncertainties stemming from statistical errors in D and the selection of $C^{(0)}$ and $A^{(0)}$ are reported in Table 2.

The final red pebble end-member composition exhibits elevated Al$_2$O$_3$ (10.49 ± 0.19 wt %) and SiO$_2$ (55.39 ± 0.97 wt %) concentrations and depleted FeO (10.01 ± 0.29 wt %) and MgO (5.74 ± 0.14 wt %) concentrations relative to Mars average soil reported in Taylor and McLennan (2009) (Tables 1, 2, and Figure 10). This end-member is closest in composition to George Drouillard targets (particularly targets one and two, which are centered over the red pebbles as opposed to the third observation), where the APXS FOVs are dominated by red pebbles (Figures 4 and 5). The bright soil clod end-member is enriched in S and Ni and is depleted in Si, relative to Mars average soil reported in Taylor and McLennan (2009). The high S abundance of the soil clod end-member is consistent with the S-rich compositions of the E Cann targets (Table 1 and Figure 4). In fact, the composition is closest to the first two Joseph Field observations, which were centered over the Pancam spectral end-member soil clod relative to the Joseph Field-3 and Joseph Field-4 observations (Figures 4 and 5b). The dark pebble end-member composition is the most similar of the three end-members to Mars average soil, although slightly enriched in S and Fe relative to that standard.

4. Testing the Validity of the Compositional End-Members

One test of the validity of the end-member compositions and the overall approach of assuming that Pancam-based spectral end-members correspond to APXS composition end-members is to place the data in the context of the complete set of compositions for Spirit of Saint Louis Crater and Marathon Valley (e.g., Mittlefehldt et al., 2016). We show the ensemble of major element data in a correspondence analysis plot in which oxide abundances and targets are normalized so that variance and samples can be displayed with the same factor loadings (Figure 11) (Larsen et al., 2000). The first two factor loadings capture 88% of the variance in the total data set. We have also examined data in the first three factor loadings and found that the dominant trends are well expressed in the first two loadings. In the swarm of data projected onto the first two loadings, the red pebble compositional end-member plots close to compositions estimated from APXS observations with extensive red pebble coverage, together with showing affinities for Si and Al. The soil clod end-member plots along a vector that extends from E Cann and Joseph Field data, but is more extreme, with affinities for Mg and S. The dark pebble end-member also plots on an extremum of the data swarm, with an affinity for Fe and Mn and a slight displacement toward increased S relative to average Mars soil. This displacement is also away from the Joseph Collin target composition, which is a fresh wind-blown deposit of basaltic sand in Marathon Valley. The target Joseph Field_3, which has the least areal coverage of the soil clod, plots between the dark and red pebble end-member locations, consistent with the APXS coverage of small dark pebbles and red soil for this observation. Likewise, the George Drouillard_3 target, which has the least areal coverage of red pebbles among the three George Drouillard targets, falls between the red and dark pebble end-member locations, again consistent with the increased areal extent of small dark pebbles relative to the other two George Drouillard targets. We conclude that the end-members retrieved using our methodology are compositionally reasonable and consistent with areal exposures sampled by the APXS FOVs.
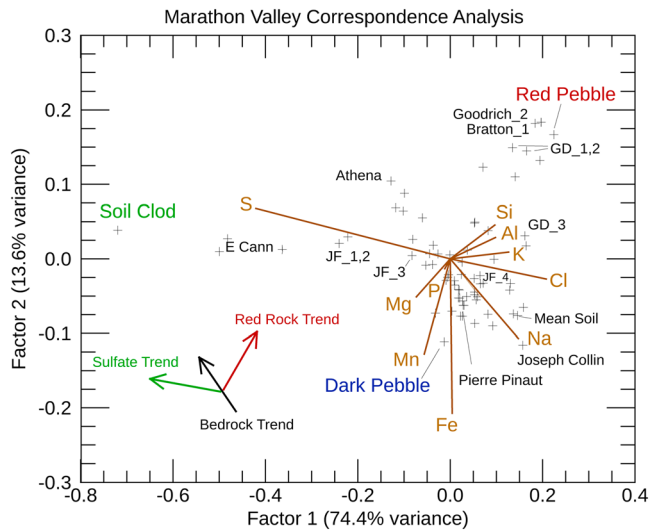
Figure 11. Correspondence analysis for the first two factor loadings for Marathon Valley observations. The soil clod end-member is clearly characterized by an affinity for S and smaller quantities of Mg. The red pebble compositional end-member is characterized by an affinity for Si and Al and plots within the field of red pebble measurements Goodrich_2, Bratton_2, and Cruzat_1, in addition to the George Drouillard series. The soil clod end-member extends along a vector connecting the E Cann and Joseph Field set of measurements and likely shows the actual sulfate-rich end-member composition of the scuffed soil. The dark pebble end-member location is similar to Mars average soil but displaced toward Fe and Mn. The ensemble of data for Marathon Valley indicates three trends of aqueous alteration: from relatively unaltered rock to the S-rich Athens bedrock (Mittlefehldt et al., 2016), formation of red pebbles, and sulfate-rich soil. The latter two trends are discussed in this paper.

The question then becomes whether the three end-members fit within an overall geochemical trend associated with Spirit of Saint Louis Crater and Marathon Valley. We infer from the correspondence analysis plot (Figure 11) the presence of three alteration trends: a generation of high Si- and Al-bearing red pebbles, sulfate-cemented soils within fractures, and a third trend evident in the swarm of bedrock observations that have as one extreme the Athena target on the southern edge of the apron surrounding the Spirit of Saint Louis Crater and the ensemble of Pierre Pinaut targets within Marathon Valley. Although beyond the scope of this paper, the bedrock trend is clearly distinct from the red pebble and sulfate-rich trends within fractures and will be the focus of future work.

An additional evaluation of the viability of the compositional end-members is to evaluate whether the composition of the soil clod end-member corresponds with a plausible mineral assemblage. To test this idea, we first model the clod as an evaporative deposit. The elemental components of the soil clod end-member were added to pure water in a thermodynamic model with the resulting mineral products predicted by equilibrium solubility conditions. Two kilograms of elements as their oxide equivalents were reacted with 1 kg of water in the model. The resulting fluid contained substantial dissolved components, and evaporation was thus simulated in a second step to induce full mineral precipitation. Calculations were performed in the Geochemist's Workbench 11.0.6 (Bethke, 2007) using the Lawrence Livermore Thermochemical Database (Delany & Lundeen, 1990) for the initial calculations and a Pitzer-style database (Harvie et al., 1984) for the evaporation calculations. Modifications made to both databases to include updated solubility, complexation, and activity data that have been recently described in Liu and Catalano 2016. For all calculations, conditions were assumed to be oxidizing and iron was solely in the ferric (Fe^{3+}) form. Mineral products were limited to phases known to form rapidly from aqueous solutions as the high sulfate content suggests evaporative conditions. P, Ti, Cr, and Mn were only considered during the initial calculations because data are lacking to consider these in a Pitzer-style evaporative model. Less than 0.1% of each of these elements remained in the fluid at the end of the first step, and the compositional limitations of the evaporative stage of the modeling thus did not affect the final mineral assemblages. Ni, Zn, and Br were not included in the calculation because of their low abundances in comparison to the major elements and their expected occurrence substituting in other phases, for example, Ni is expected to occur as a trace impurity in sulfates or oxide minerals.

The calculations produced an assemblage consisting of >40 wt % Mg sulfate (as epsomite), with the other major components consisting of amorphous silica, schwertmannite, gypsum, and aluminum sulfate phases (Figure 12). Minor components consisted of a variety of phosphate, oxide, and salt minerals. This assemblage was associated with a fluid having a pH initially around 3.8 that dropped to 0.7 during evaporation. The mineral products and fluid behavior did not vary substantially in preliminary calculations when clays or crystalline iron oxides were allowed to form, other than the dominant iron mineral changed from schwertmannite to nontronite, or hematite, with Mg sulfate still occurring as the dominant phase at >40 wt %. Allowing quartz to form simply resulted in this
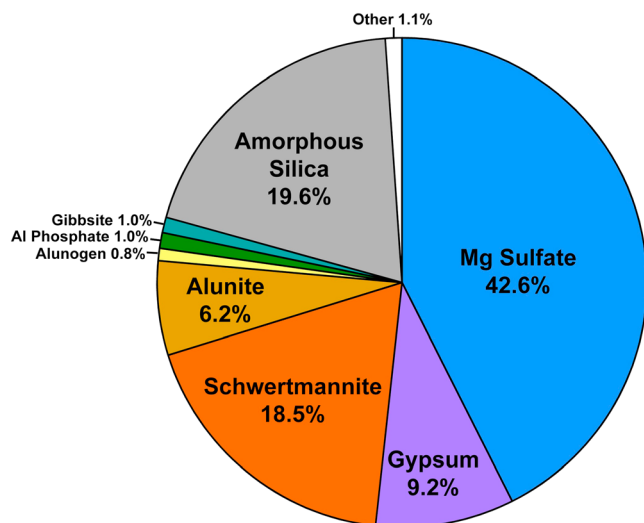

Figure 12. Mineral abundance of the soil clod end-member predicted via thermo-dynamic modeling.

mineral occurring instead of amorphous silica. It is possible, and perhaps likely, that the soil clod contains basaltic grains cemented by sulfate-rich phases. We also considered such models with varying amounts of basaltic materials and came to the same general conclusion that sulfate phases would dominate the evaporative component.

The highly acidic and oxidizing nature of the final fluid results from the high iron content, the assumption is that iron is purely in the ferric form, the large S component, and the known acidifying effect of high degrees of evaporation (Tosca et al., 2005). Producing a circumneutral final fluid requires ~25% lower sulfur content or ~75% of the iron to be in the ferrous (Fe^{2+}) form. Together, these calculations suggest that the soil clod end-member is the product of alteration and leaching of underlying rock by an acidic, sulfate-rich fluid, followed by evaporation within the fracture zone, consistent with known geochemical processes on Mars. Further, we propose that the oxidizing conditions in place during this process led to leaching, disaggregation, and oxidation of the rocks now present as the cluster of red pebbles within the fracture zone.

5. Conclusions and Implications

A log maximum likelihood iterative method has been implemented to determine the oxide abundances of compositional end-members in a soil-filled fracture in Marathon Valley on the Cape Tribulation rim segment of the 22 km wide, Noachian-age Endeavour crater. Marathon Valley was the site of extensive measurements by the Opportunity rover including a soil-filled fracture scuffed by dragging the rover's left front wheel. Colorful subsurface soil was exposed during the scuff motions. Ten Alpha Particle X-ray Spectrometer (APXS) measurements within and near the scuff were convolved with spectral reflectance areal abundance end-member maps derived from Pancam 13 filter images covering ~0.4 to 1.0 μm in wavelength. A log maximum likelihood iterative method was used to solve for the compositions of the three relatively pure Pancam-based spectral end-member locations, thereby sharpening the compositional estimates to the components that make up the scuff and nearby areas. The approach of assuming Pancam-based spectral end-members correspond to realistic compositional end-members was validated using several approaches in this paper.

The first compositional end-member corresponds to a cluster of red pebbles within the fracture zone, with Pancam-based evidence of a slight enrichment in nanophase iron oxide, and a composition enriched in Al, Si, and K and depleted in Fe and Mg relative to Mars average soil. The second is a soil clod end-member exposed by the wheel scuff. It is enriched in Mg, S, and Ni and depleted in Al and Si relative to Mars average soil. The third end-member is a dark pebble end-member similar in composition to Mars average soil, with minor enrichments in S and Fe. The soil clod end-member is interpreted to be the evaporative product of fluids produced by alteration and leaching in an acidic, sulfate-rich environment with enhanced flow along fractures. The evaporative minerals cemented basaltic soils filling the fracture. Further, the leached and oxidized nature of the red pebbles likely results from alteration in this acidic environment.

These results are consistent with other evidence from Opportunity and CRISM that broadly signals pervasive aqueous alteration along the rim of Endeavour crater. Observations in the pre-Endeavour Matijevic formation rocks of Fe^{+3}-rich smectite and relatively high concentrations of Al-rich clays and hydrated silica-rich materials suggest aqueous alteration that was enhanced by fluid flow along fractures and interpreted to occur in reducing fluid (Arvidson et al., 2014). In Cook Haven on the northern portion of the Murray Ridge, Opportunity observed sulfate-rich coatings and one or more Mn oxide phases on basaltic rocks, consistent with authigenic mineral deposition involving the precipitation of sulfates from subsurface fluids that likely came into contact with an oxidizing surface environment (Arvidson et al., 2016). CRISM-based observations of Fe^{3+}-Mg^{2+} smectite in the planar outcrops in Marathon Valley provide evidence of subsurface alteration of the basaltic Noachian crust (Fox et al., 2016). The results from the Marathon Valley scuff zone are consistent with previous evidence of alteration that was concentrated along fractures, which likely provided a conduit for subsurface fluid flow. The timing of the formation of these deposits is unclear; they could have formed as sulfate-bearing fluids evaporated during transient postimpact hydrothermal activity or perhaps during the emplacement of the Burns formation utilizing groundwater from the southern highlands.

References

Arvidson, R. E., Squyres, S. W., Bell, J. F., Catalano, J. G., Clark, B. C., Crumpler, L. S., … Wolff, M. J. (2014). Ancient aqueous environments at Endeavour Crater, Mars. *Science, 343*(6169), 1248097. https://doi.org/10.1126/science.1248097

Arvidson, R. E., Squyres, S. W., Morris, R. V., Knoll, A. H., Gellert, R., Clark, B. C., … de Souza, P. A. Jr. (2016). High concentrations of manganese and sulfur in deposits on Murray ridge, Endeavour crater, Mars. *American Mineralogist, 101*(6), 1389–1405. https://doi.org/10.2138/am-2016-5599

Bell, J. F. III, Joseph, J., Sohl-Dickstein, J. N., Arneson, H. M., Johnson, M. J., Kemmon, M. T., & Savransky, D. (2006). In-flight calibration and performance of the Mars Exploration Rover Panoramic Camera (Pancam) instruments. *Journal of Geophysical Research, 111*, E02S03. https://doi.org/10.1029/2005JE002444

Bethke, C. M. (2007). *Geochemical and biogeochemical reaction modeling* (p. 546). Cambridge: Cambridge University Press. https://doi.org/10.1017/CBO9780511619670

Crumpler, L. S., Arvidson, R. E., Mittlefehldt, D. W., Jolliff, B. L., Farrand, W. H., Fox, V., … Golombek, M. P. (2016). Opportunity, geologic and structural context of aqueous alteration in Noachian outcrops, Marathon Valley, rim of Endeavour crater. *LPSC 47*. Abstract 2272.

Csiszár, I. (1991). Why least squares and maximum entropy? An axiomatic approach to inference for linear inverse problems. *Annals of Statistics, 19*(4), 2032–2066. https://doi.org/10.1214/aos/1176348385

Delany, J. M., & Lundeen, S. R. (1990). The LLNL thermochemical database (p. 150). Lawrence Livermore National Laboratory.

Farrand, W. H., Johnson, J. R., Rice, M. S., Wang, A., & Bell, J. F. III (2016). VNIR multispectral observations of aqueous alteration materials by the Pancams on the Spirit and Opportunity Mars Exploration Rovers. *American Mineralogist, 101*(9), 2005–2019. https://doi.org/10.2138/am-2016-5627

Farrand, W.H., Johnson, J. R., Bell, J. F. III, Mittlefehldt, D. W., Gellert, R., VanBommel, S., … Schroder, C. (2017). Pancam multispectral and APXS chemical examination of rocks and soils in Marathon Valley and points south along the rim of Endeavour crater. *LPSC 48*. Abstract 2453.

Fox, V. K., Arvidson, R. E., Guinness, E. A., McLennan, S. M., Catalano, J. G., Murchie, S. L., & Powell, K. E. (2016). Smectite deposits in Marathon Valley, Endeavour crater, Mars, identified using CRISM hyperspectral reflectance data. *Geophysical Research Letters, 43*, 4885–4892. https://doi.org/10.1002/2016GL069108

Gellert, R., Rieder, R., Brückner, J., Clark, B. C., Dreibus, G., Klingelhöfer, G., … Squyres, S. W. (2006). Alpha particle X-ray spectrometer (APXS): Results from Gusev crater and calibration report. *Journal of Geophysical Research, 111*, E02S05. https://doi.org/10.1029/2005JE002555

Gorevan, S. P., Myrick, T., Davis, K., Chau, J. J., Bartlett, P., Mukherjee, S., … Richter, L. (2003). Rock abrasion tool: Mars Exploration Rover mission. *Journal of Geophysical Research, 108*(E12) 8068. https://doi.org/10.1029/2003JE002061

Harvie, C. E., Møller, N., & Weare, J. H. (1984). The prediction of mineral solubilities in natural waters: The Na-K-Mg-Ca-H-Cl-SO$_4$-OH-HCO$_3$-CO$_3$-CO$_2$-H$_2$O system to high ionic strengths at 25°C. *Geochimica et Cosmochimica Acta, 48*(4), 723–751. https://doi.org/10.1016/0016-7037(84)90098-X

Herkenhoff, K. E., Squyres, S. W., Bell, J. F. III, Maki, J. N., Arneson, H. M., Bertelsen, P., … Wadsworth, M. V. (2003). Athena Microscopic Imager investigation. *Journal of Geophysical Research, 108*(E12), 8065. https://doi.org/10.1029/2003JE002076

Larsen, K. W., Arvidson, R. E., Jolliff, B. L., & Clark, B. C. (2000). Correspondence and least squares analyses of soil and rock compositions for the Viking Lander 1 and Pathfinder landing sites. *Journal of Geophysical Research, 105*(E12), 29,207–29,221. https://doi.org/10.1029/2000JE001245

Lee, D. D., & Seung, H. S. (1999). Learning the parts of objects by non-negative matrix factorization. *Nature, 401*(6755), 788–791. https://doi.org/10.1038/44565

Lee, D. D., & Seung, H. S. (2001). Algorithms for non-negative matrix factorization. In *Advances in neural information processing systems* (Vol. 13, pp. 556–562).

Liu, Y., & Catalano, J. G. (2016). Implications for the aqueous history of southwest Melas Chasma, Mars as revealed by interbedded hydrated sulfate and Fe/Mg-smectite deposits. *Icarus, 271*, 283–291. https://doi.org/10.1016/j.icarus.2016.02.015

Malin, M. C., Bell, J. F. III, Cantor, B. A., Caplinger, M. A., Calvin, W. M., Clancy, R. T., … Wolff, M. J. (2007). Context camera investigation on board the Mars Reconnaissance Orbiter. *Journal of Geophysical Research, 112*, E05S04. https://doi.org/10.1029/2006JE002808

McEwen, A. S., Eliason, E. M., Bergstrom, J. W., Bridges, N. T., Hansen, C. J., Delamere, W. A., … Weitz, C. M. (2007). Mars Reconnaissance Orbiter's High Resolution Imaging Science Experiment (HiRISE). *Journal of Geophysical Research, 112*, E05S02. https://doi.org/10.1029/2005JE002605

Mittlefehldt, D. W., Gellert, R., Van Bommel, S., Arvidson, R. E., Clark, B. C., Ming, D. W., … Jolliff, B. L., (2016). Alumina + silica + germanium alteration in smectite-bearing Marathon Valley, Endeavour crater rim, Mars. *LPSC 47*. Abstract 2086.

O'Sullivan, J. A. (2000). Properties of the information value decomposition. *Information Theory, 2000. Proceedings. IEEE International Symposium*.

Squyres, S. W., Arvidson, R. E., Bell, J. F., Calef, F., Clark, B. C., Cohen, B. A., … Zacny, K. (2012). Ancient impact and aqueous processes at Endeavour crater, Mars. *Science, 336*(6081), 570–576. https://doi.org/10.1126/science.1220476

Taylor, S. R., & McLennan, S. M. (2009). *Planetary crusts: Their composition, origin, and evolution*. New York: Cambridge University Press.

Tosca, N. J., McLennan, S. M., Clark, B. C., Grotzinger, J. P., Hurowitz, J. A., Knoll, A. H., … Squyres, S. W. (2005). Geochemical modeling of evaporation processes on Mars: Insight from the sedimentary record at Meridiani Planum. *Earth and Planetary Science Letters, 240*(1), 122–148. https://doi.org/10.1016/j.epsl.2005.09.042

VanBommel, S. J., Gellert, R., Berger, J. A., Campbell, J. L., Thompson, L. M., Edgett, K. S., … Boyd, N. I. (2016). Deconvolution of distinct lithology chemistry through oversampling with the Mars Science Laboratory Alpha Particle X-ray Spectrometer. *X-Ray Spectrometry, 45*(3), 155–161. https://doi.org/10.1002/xrs.2681

VanBommel, S. J., Gellert, R., Berger, J. A., Thompson, L. M., Edgett, K. S., McBride, M. J., … Campbell, J. L. (2017). Modeling and mitigation of sample relief effects applied to chemistry measurements by the Mars Science Laboratory Alpha Particle X-ray Spectrometer. *X-Ray Spectrometry, 46*(4), 229–236. https://doi.org/10.1002/xrs.2755